Supporting Information for:

First-Row Transition Metal Complexes of a New Pentadentate Ligand, α,α,α',α'-Tetra(pyrazolyl)lutidine.

Tyler J. Morin, Sergey V. Lindeman, James R. Gardinier*

Department of Chemistry, Marquette University, Milwaukee WI, 53201-1881

Email: james.gardinier@marquette.edu.

Table of Contents:

Experimental.

General Considerations. Pyrazole, thionyl chloride, NaH, and all transition metal halides were obtained commercially and were used as received. The compound 2,6-pyridinedicarboxaldehyde was prepared according to a literature method. Solvents were dried by conventional procedures and distilled prior to use, except where noted. Midwest MicroLab, LLC, Indianapolis, Indiana 45250, performed all elemental analyses. Melting point determinations were made on samples contained in glass capillaries using an Electrothermal 9100 apparatus and are uncorrected. ^{1}H and ^{13}C NMR spectra were recorded on a Varian 300 MHz spectrometer. Chemical shifts were referenced to solvent resonances at δ_H 7.27 and δ_C 77.23 for $CDCl_3$, δ_H 3.31 and δ_C 49.15 for methanol-d_4. UV-visible and NIR spectra were recorded using Shimadzu UV-1600/1700 or Jasco V-570 instruments. Solid-state magnetic measurements were made at room temperature using an MK1 magnetic susceptibility balance. EPR spectral measurements were obtained using a Bruker ELEXSYS E600 equipped with an ER4116DM cavity resonating at 9.63 GHz, an Oxford Instruments ITC503 temperature controller and ESR-900 helium flow cryostat. The ESR spectra were recorded with 100 kHz field modulation.

Syntheses.

α, α, α', α'- tetra(pyrazolyl)lutidine, pz_4lut. A mixture of 50.2 mmol $SO(pz)_2$ [generated in-situ from 2.50 g (104 mmol) NaH, 7.08 g (104 mmol) pyrazole and 3.66 ml (5.97 g, 50.2 mmol) $SOCl_2$ in 200 mL THF], 3.35 g (24.8 mmol) 2,6-pyridinedicarboxaldehyde and 0.805 g (6.20 mmol, 30 mol%) $CoCl_2$ (added as solids under N_2) were heated at reflux 20 h. The reaction mixture was then allowed to cool to room temperature and 100 mL of each H_2O and CH_2Cl_2 was carefully added. The aqueous and organic layers were separated. The pink aqueous layer was extracted with three 50 mL portions CH_2Cl_2 and the combined organics were dried over $MgSO_4$, filtered and solvent was removed to leave a brown oily

residue. Chromatographic separation using neutral alumina with diethyl ether as an eluent afforded crude pz_4lut as a colorless powder from the second band (R_f = 0.68, Al_2O_3 plate)**.** Colorless crystals 3.78 g (41 %) of pure pz_4lut were obtained after layering an acetone solution with hexanes, allowing the solvents to slowly diffuse over 2 d, filtering, and drying. Mp, 121-122 ^{o}C. Anal. Calcd. (obsd.) for $C_{19}H_{17}N_9$: C, 61.44 (61.07); H, 4.61 (4.92); N, 33.94 (33.71). ^{1}H NMR ($CDCl_3$) δ_H 7.74 (t, *J* = 8 Hz, 1H, H_4-py), 7.71 (s, 2H, $CHpz_2$), 7.57 (d, *J* = 1 Hz, 4H, H_3-pz), 7.52 (d, *J* = 2 Hz, 4H, H_5-pz), 7.12 (d, *J* = 8 Hz, 2H, $H_{3/5}$-py), 6.27 (dd, *J* = 2,1 Hz, 4H, H_4-pz). ^{13}C NMR ($CDCl_3$) δ_C 154.7, 140.9, 138.8, 129.9, 122.9, 106.8, 78.0. UV-Vis (Methanol) λ_{max}, nm (ε, M^{-1}, cm^{-1}) 217 (30,637), 263 (6693).

[MnCl(pz_4lut)](Cl)•CH_2Cl_2, 1•CH_2Cl_2. A solution of 0.191 g (0.514 mmol) of **pz_4lut** in 8.5 mL dichloromethane was layered with a methanol solution (8.5 mL) of 0.108 g (0.546 mmol) $MnCl_2{\cdot}4H_2O$. After 3 days, 0.176 g (59 %) of X-ray quality colorless blocks of **1**•CH_2Cl_2 were collected after filtration, washing with Et_2O and drying under vacuum. Mp, 190-195 ^{o}C, dec. Anal. Calcd. (found) for $C_{20}H_{19}Cl_4MnN_9$: C, 41.26 (41.22); H, 3.29 (3.46); N, 21.65 (21.96). μ_{eff} (Evans) (CD_3OD, 298 K) 5.9 μ_B. UV-Vis (MeOH) λ_{max}, nm (ε, M^{-1}, cm^{-1}), 215 (29404), 264 (5614), 342 (53).

[FeCl(pz_4lut)](Cl)•CH_2Cl_2, 2•CH_2Cl_2. A solution of 0.100 g (0.789 mmol) of $FeCl_2$ in 8.5 mL of MeOH was layered onto a solution of 0.293 g (0.789 mmol) **pz_4lut** in 8.5 mL of CH_2Cl_2. After 3 days, 0.450 g (98 %) of orange X-ray quality crystals of **2**•CH_2Cl_2 were collected as above. Mp, 247-257 ^{o}C dec. Anal. Calcd. (found) for $C_{20}H_{19}Cl_4FeN_9$: C, 41.20 (41.59); 3.28 (3.50); 21.62 (21.68). μ_{eff} (Evans) (CD_3OD, 298 K) 5.2 μ_B. UV-Vis (MeOH) λ_{max}, nm (ε, M^{-1}, cm^{-1}), 263 (8762), 300 (2677), 428 (282), 888 (19). 1050sh (10).

[CoCl(pz$_4$lut)](Cl)•CH$_2$Cl$_2$, 3•CH$_2$Cl$_2$. A solution of 0.286 g (0.770 mmol) **pz$_4$lut** in 8.5 mL of CH_2Cl_2 was layered with a solution of 0.105 g (0.809 mmol) $CoCl_2$ in 8.5 mL MeOH and solvents were allowed to slowly diffuse over 3 days. A 0.405 g (90 %) sample of **3**•CH_2Cl_2 as pink X-ray quality crystals was collected and dried under vacuum. Mp, 282-285 ^{o}C dec. Anal. Calcd. (found) for $C_{20}H_{19}Cl_4CoN_9$; C, 40.98 (40.95); H, 3.27 (3.29); N, 21.51 (21.49). μ_{eff} (solid) 3.6 μ_B. UV-Vis (CH_3OH) λ_{max}, nm (ε, M^{-1}, cm^{-1}), 264 (4936), 300sh (608), 472 (20), 934 (4).

[NiCl(pz$_4$lut)](Cl), 4. A chloroform (8.5 mL) solution of 0.161 g (0.433 mmol) **pz$_4$lut** was layered with a ethanol (8.5 mL) solution of 0.106 g (0.446 mmol) of $NiCl_2 \cdot 6H_2O$. After the solvents were allowed to diffuse for 3 d, 0.243 g (98 %) of violet microcrystalline **4**, was isolated after filtration and drying under vacuum. Mp, 200-203 ^{o}C, dec. Anal. Calcd. (found) for $C_{19}H_{17}Cl_2N_9Ni$: C, 45.55 (45.31); H, 3.42 (3.24); N, 25.16 (25.04). μ_{eff} (solid) 2.3 μ_B. UV-Vis (CH_3OH) λ_{max}, nm (ε, M^{-1}, cm^{-1}), 268 (3455), 300sh (188), 563 (25), 764sh (7), 874 (13). X-ray quality crystals of a solvate (**4**•EtOH) are obtained before drying. The solvent is readily removed by vacuum.

[CuCl(pz$_4$lut)](Cl), **5.** A solution containing 0.169 g (0.45 mmol) **pz$_4$lut** in 8.5 mL CH_2Cl_2 was layered with a methanol (8.5 mL) solution of 0.063 g (0.47 mmol) $CuCl_2$ and solvents were allowed to diffuse over 3 days. A 0.216 g (95 %) sample of **5** as a green microcrystalline powder was collected by filtration and dried under vacuum. Mp, 267-270 ^{o}C, dec. Anal. Calcd. (Obsd.) for $C_{19}H_{17}Cl_2CuN_9$: C, 45.11 (45.85); H, 3.39 (3.00); N, 24.92 (24.56). μ_{eff} (solid) 2.3 μ_B. UV-Vis (CH_3OH) λ_{max}, nm (ε, M^{-1}, cm^{-1}), 270(3611), 424(278), 700 (43), 1150sh (12). X-ray quality crystals of a solvate (**5**•0.82 CH_2Cl_2) are obtained before drying. The solvent is readily removed by vacuum.

[ZnCl(pz_4lut)][$ZnCl_3$(MeOH)] 6. A dichloromethane (8.5 mL) solution containing 0.276 g (0.743 mmol) **pz_4lut** was layered with a methanol (8.5 mL) solution containing 0.109 g (0.800 mmol) of $ZnCl_2$. After allowing the solvents to diffuse over 4 days, 0.253 g (89 % based on $ZnCl_2$) of **6** were collected by filtration and dried under vacuum. Mp, 284-290 ^{o}C, dec. Anal. Calcd. (found) for $C_{20}H_{21}Cl_4N_9OZn_2$: C, 35.53 (35.15); H, 3.13 (3.43); N, 18.65 (18.28). This compound is surprisingly less soluble in CD_3OD, than in CH_3OH in which the complex has sparing solubility (it is also insoluble in all other typical organic solvents), so ^{1}H NMR were recorded as a saturated solution 10 vol-% D_2O in CD_3OD while ^{13}C NMR spectral data could not be recorded in a reasonable amount of acquisition time. ^{1}H NMR (CD_3OD/10 vol-% D_2O) δ_H 8.32 (br s, 4H), 8.27-8.23 (br m, 6H), 8.09 (br m, 3H), 6.57 (s, 4H, H_4-pz). X-ray quality crystals of a solvate (**6**•0.63 CH_2Cl_2•0.34 MeOH) are obtained before drying. The solvent is readily removed by vacuum. UV-Vis (CH_3OH) λ_{max}, nm (ε, M^{-1}, cm^{-1}), 216 (25,271), 264 (5,736), 300sh (1008).

Crystal Structure Determinations.

General considerations. X-ray intensity data from a colorless block of [MnCl(**pz$_4$lut**)](Cl)•CH_2Cl_2 (**1**•CH_2Cl_2), an orange block of [FeCl(**pz$_4$lut**)](Cl)•CH_2Cl_2 (**2**•CH_2Cl_2), a pink block of [CoCl(**pz$_4$lut**)](Cl)•CH_2Cl_2 (**3**•CH_2Cl_2), a violet block of [NiCl(**pz$_4$lut**)](Cl)•EtOH (**4**•EtOH), an aquamarine plate of [CuCl(**pz$_4$lut**)](Cl)•0.82CH_2Cl_2 (**5**•0.82CH_2Cl_2), and a colorless block of [ZnCl(**pz$_4$lut**)][$ZnCl_3$(MeOH)]•0.63 CH_2Cl_2•0.34 MeOH (**6**•0.63 CH_2Cl_2•0.34 MeOH) were measured at 100(2) K a Bruker AXS 3-circle diffractometer equipped with a SMART2[S1] CCD detector using Cu Kα radiation (λ = 1.54178 Å), as summarized in Table 1. Raw data frame integration and Lp corrections were performed with SAINT+.[S2] Final unit cell parameters were determined by least-squares refinement of 5863 reflections for (**1**•CH_2Cl_2), 7197 reflections for (**2**•CH_2Cl_2), 6674 reflections for (**3**•CH_2Cl_2), 5800 reflections for (**4**•EtOH), 4545 reflections for (**5**•0.82CH_2Cl_2), 9556 reflections for (**6**•0.63 CH_2Cl_2•0.34 MeOH), each with I > 2σ(I) from their respective data sets. For each, analysis of the data showed negligible crystal decay during collection. Numerical absorption corrections were applied to the data for each derivative the cobalt derivatives. Direct methods structure solutions, difference Fourier calculations and full-matrix least-squares refinements against F^2 were performed with SHELXTL.[S2] The crystals of **1**•CH_2Cl_2 **2**•CH_2Cl_2 **3**•CH_2Cl_2 and **4**•EtOH were pseudo-orthorhombic twins consisting of two monoclinic components (68:32 ratio for Co) with beta angle close to 90^o and the TWIN -1 0 0 0 -1 0 0 0 1 instruction was used during the refinements. All non-hydrogen atoms were refined with anisotropic displacement parameters. Hydrogen atoms were placed in geometrically idealized positions and included as riding atoms.

[S1] SMART Version 5.630, SAINT+ Version 6.45, and SADABS Version 2.05. Bruker Analytical X-ray Systems, Inc., Madison, Wisconsin, USA, 2003.

[S2] Sheldrick, G. M. SHELXTL Version 6.14; Bruker Analytical X-ray Systems, Inc., Madison, Wisconsin, USA, 2000.

Table S1. Crystallographic Data and Refinement Parameters for (a) [MnCl(**pz$_4$lut**)](Cl)•CH_2Cl_2 (**1**•CH_2Cl_2); (b) [FeCl(**pz$_4$lut**)](Cl)•CH_2Cl_2 (**2**•CH_2Cl_2); (c) [CoCl(**pz$_4$lut**)](Cl)•CH_2Cl_2 (**3**•CH_2Cl_2); (d) [NiCl(**pz$_4$lut**)](Cl)•EtOH (**4**•EtOH), (e) [CuCl(**pz$_4$lut**)](Cl)•0.82CH_2Cl_2 (**5**•0.82CH_2Cl_2), (f) [ZnCl(**pz$_4$lut**)][$ZnCl_3$(MeOH)]•0.63 CH_2Cl_2•0.34 MeOH (**6**•0.63 CH_2Cl_2•0.34 MeOH).

Compound	**1**•CH_2Cl_2	**2**•CH_2Cl_2	**3**•CH_2Cl_2	**4**•EtOH	**5**•0.82 CH_2Cl_2	**6**•0.63 CH_2Cl_2•0.34 MeOH
Formula	$C_{20}H_{19}Cl_4MnN_9$	$C_{20}H_{19}Cl_4FeN_9$	$C_{20}H_{19}Cl_4CoN_9$	$C_{21}H_{23}Cl_2N_9NiO$	$C_{19.82}H_{18.65}Cl_{3.64}CuN_9$	$C_{21.37}H_{25.21}Cl_{5.26}N_9O_{1.74}Zn_2$
Formula weight	582.18	583.09	586.17	547.09	575.71	753.22
Crystal system	Monoclinic	Monoclinic	Monoclinic	Monoclinic	Monoclinic	Monoclinic
Space Group	$P2_1/n$	$P2_1/c$	$P2_1/n$	C2/c	$P2_1/c$	$P2_1/n$
a, Å	10.5304(6)	10.4115(5)	10.2900(2)	21.7305(7)	10.8339(2)	11.52640(10)
b, Å	19.2722(10)	19.2410(9)	19.1675(3)	22.0929(8)	22.2728(3)	13.94720(10)
c, Å	11.9444(6)	12.0005(6)	12.0572(2)	9.7949(4)	9.80290(10)	18.9316(2)
β, deg	90.000(2)	90.000(2)	90.0330(10)	90.0000(10)	92.9950(10)	102.3930(10)
V, $Å^3$	2424.0(2)	2404.0(2)	2378.08(7)	3156.57(6)	2362.22(6)	2972.55(5)
Z	4	4	4	8	4	4
T, K	100(2)	100(2)	100(2)	100(2)	100(2)	100(2)
ρ calcd, Mg m^{-3}	1.595	1.611	1.637	1.546	1.619	1.683
λ, Å	1.54178	1.54178	1.54178	1.54178	1.54178	1.54178
μ (Cu Kα), mm^{-1}	8.734	9.372	10.046	3.573	5.345	6.653
R[I>2σ(I)][a](all data)	0.0473 (0.0483)	0.0353 (0.0387)	0.0411 (0.0418)	0.0366 (0.0381)	0.0311 (0.0410)	0.0237 (0.0240)
wR^b (all data)	0.1102 (0.1108)	0.0862 (0.0874)	0.1126 (0.1131)	0.0930 (0.0940)	0.0745 (0.0792)	0.0623 (0.0624)

[a] $R = \Sigma||F_o|-||F_c||/\Sigma|F_o|$. [b] $wR = [\Sigma w(|F_o^2|-|F_c^2|)^2/\Sigma w|F_o^2|^2]^{1/2}$

Table S2. Intracationic Geometric Parameters for $[MCl(\mathbf{pz_4lut})]^+$ (M = Mn, Fe, Co, Ni, Cu, Zn).

M =	Mn	Fe	Co	Ni	Cu	Zn
M-Cl (Å)	2.365	2.307	2.323	2.360	2.279	2.334
M-$N1_{py}$ (Å)	2.364	2.300	2.221	2.099	2.109	2.256
M-$N3_{pz}$ (Å)	2.237	2.179	2.140	2.088	1.999	2.163
M-$N5_{pz}$ (Å)	2.257	2.187	2.138	2.098	2.376	2.159
M-$N7_{pz}$ (Å)	2.255	2.198	2.144	2.098	2.408	2.121
M-$N9_{pz}$ (Å)	2.293	2.222	2.176	2.104	1.998	2.169
Avg. axial (Å)	2.365	2.304	2.272	2.230	2.194	2.295
Avg. Eq. (Å)	2.261	2.197	2.150	2.097	2.195	2.153
Avg. total (Å)	2.295	2.233	2.190	2.141	2.195	2.200
M-N_4pl (Å)	0.451	0.392	0.283	0.165	0.242	0.322
MN3-N2C6 (^{o})	1.50	1.93	1.22	0.58	3.55	3.27
MN5-N4C6 (^{o})	3.97	5.08	2.07	4.60	3.65	3.75
MN7-N6C7 (^{o})	0.85	1.21	4.78	0.90	6.19	1.08
MN9-N8C7 (^{o})	6.80	7.50	4.70	0.96	2.64	7.14
Avg MN-NC (^{o})	3.28	3.93	3.19	1.76	4.01	3.81
N1-M-Cl (^{o})	179.52	179.60	179.97	177.82	177.85	173.76
Oct. Vol (Å)^3	15.421	14.279	13.688	12.930	13.723	13.786
Quad. Elong.	1.034	1.026	1.016	1.010	1.024	1.021
∠variance (^{o})^2	114.41	88.46	627.84	25.34	44.24	66.54

Structural Discussion. In the [MCl(**pz$_4$lut**)](Cl) complexes (M = Mn, Fe, Co, Ni, Cu, Zn), the metal sits above the mean plane of pyrazolyl nitrogens toward the axial chloride group. A closer examination of the geometries of the various [MCl(**pz$_4$lut**)]$^+$ cations (Table S1, Figures S1 and S2), indicates that nickel(II) provides the best 'fit' for the new ligands. Relative to other metal centers, nickel is situated closest to (0.165 Å above) the mean plane of equatorial pyrazolyl nitrogens. The metal-bound pyrazolyls experience the least amount of ring-twisting in the Ni^{II} case, defined by the average MN-NC(sp^3) torsion angle of 1.76^o (compared to MnN-NC of 3.28^o in the manganese case, for example). Also, the nickel complex exhibits the smallest octahedral volume [Volume of $MN_{4(pz)}N_{(py)}Cl$ = 12.930 Å^3] and quadratic elongation (1.010)[S3] compared to all other metals in the series. There is a regular variation in bond distances versus the number of d-electrons on traversing the series from manganese (d^5) to nickel (d^8) (Figure S1). Copper (d^9) represents the break in the trend (Figure S1a) of smaller divalent metal cations giving shorter mean bond distances, due to distortion of equatorial Cu-N bonds. The [CuCl(**pz$_4$lut**)]$^+$ cation contains two very short Cu-N(pz) (Cu-N5 and Cu-N7, avg. 1.999 Å) bonds and two long Cu-N(pz) bonds (Cu-N3 and Cu-N9, avg. 2.392 Å) giving a coordination sphere that approaches square planar (with two long Cu-N(pz) contacts). If these longer axial contacts are ignored, then the Cu-N(pyrazolyl) bonds and the weighted average of all metal-ligand bonds (2.096 Å) fall in line with other metals in the series (Figure S1b). The preference for lower coordination geometries for Cu^{2+} is well-documented and is also observed in the related square-pyramidal [CuCl(κ^4-PY5)]$^+$ cation.[S4] Usually this coordination preference is attributed to Jahn-Teller distortion due to single occupancy of degenerate e_g* orbitals. The low symmetry of the complexes in this series was expected to remove such degeneracy and this distortion was unanticipated.

References:

[S3] Robinson K.; Gibbs, G. V.; Ribbe, P. H. *Science* **1971**, *172*, 567**.**

[S4] Bebbink, R.J.M.K.; Jonas, R.T.; Goldsmith, C.R.; Stack, T.D.P. *Inorg. Chem.* **2002**, *41*, 4633.

Figure S1. Plots of bond distances as a function of d-electron count of metal in [MCl(**pz$_4$lut**)]$^+$. (a) Avg. of all groups of MN_5Cl considered (b) long Cu-N(pyrazolyl) bond distances ignored.

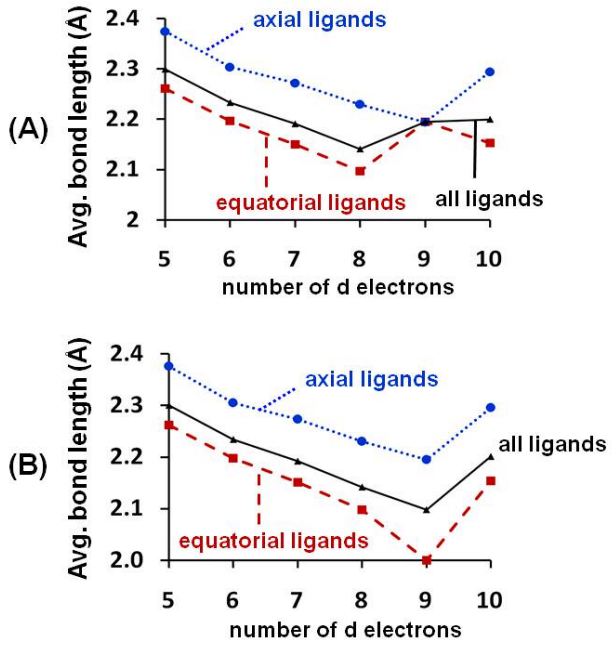

Figure S2. Plots of MN_5Cl octahedral volume (top) and deviation of M from equatorial N_4 plane (bottom) versus d- electron count of metal in [MCl(**pz$_4$lut**)]$^+$ complexes.

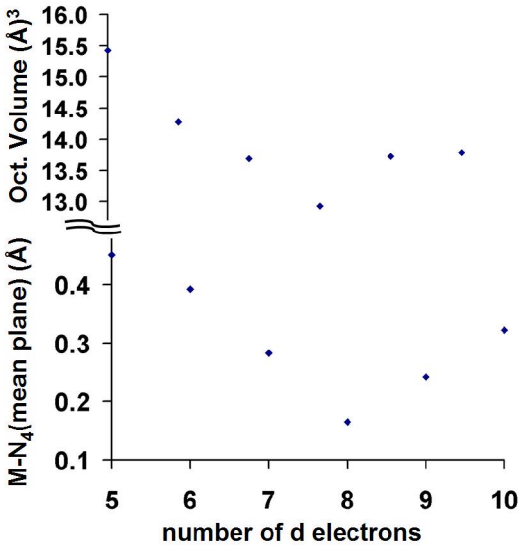

Figure S3. ORTEP diagrams (50% probability ellipsoids) of [MnCl(**pz$_4$lut**)](Cl)•CH_2Cl_2 .

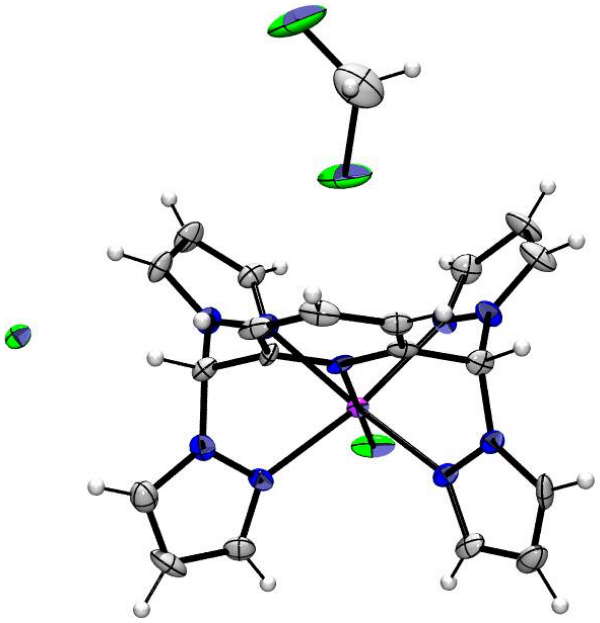

Asymmetric Unit

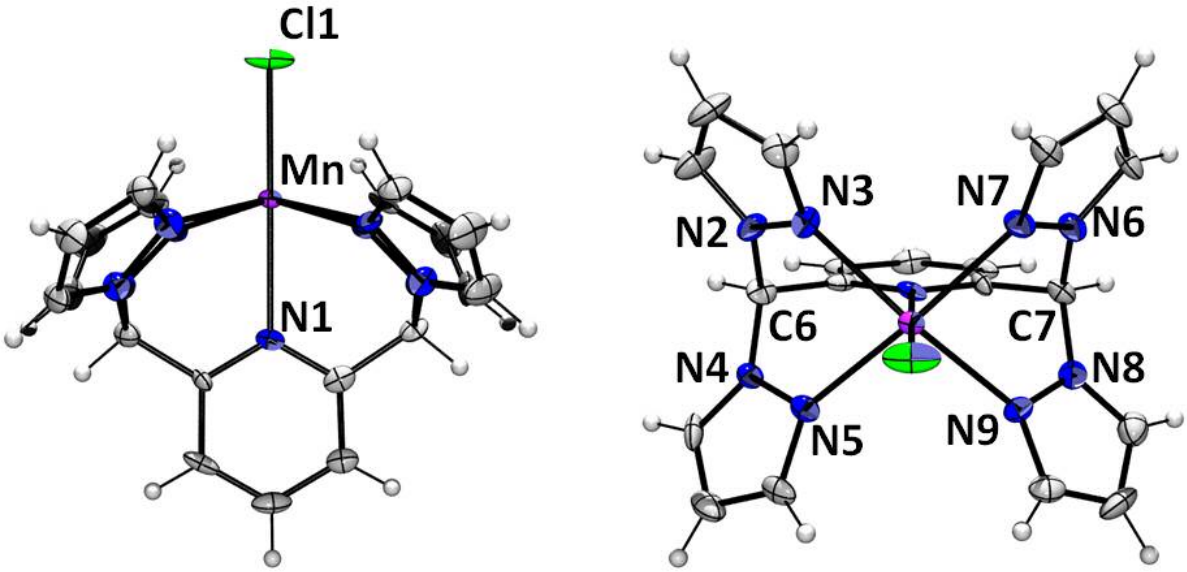

Views of Cation with Select Atom Labels

Figure S4. ORTEP diagrams (50% probability ellipsoids) of [FeCl(**pz$_4$lut**)](Cl)•CH_2Cl_2.

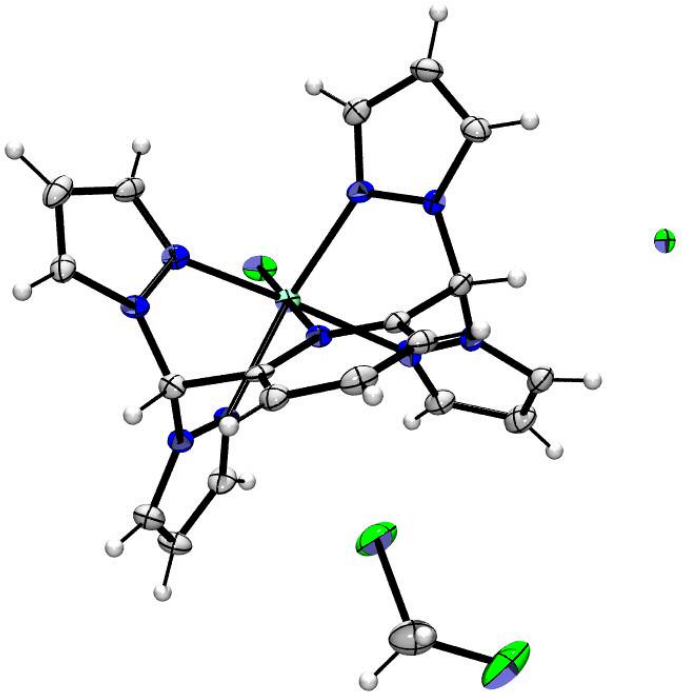

Asymmetric Unit

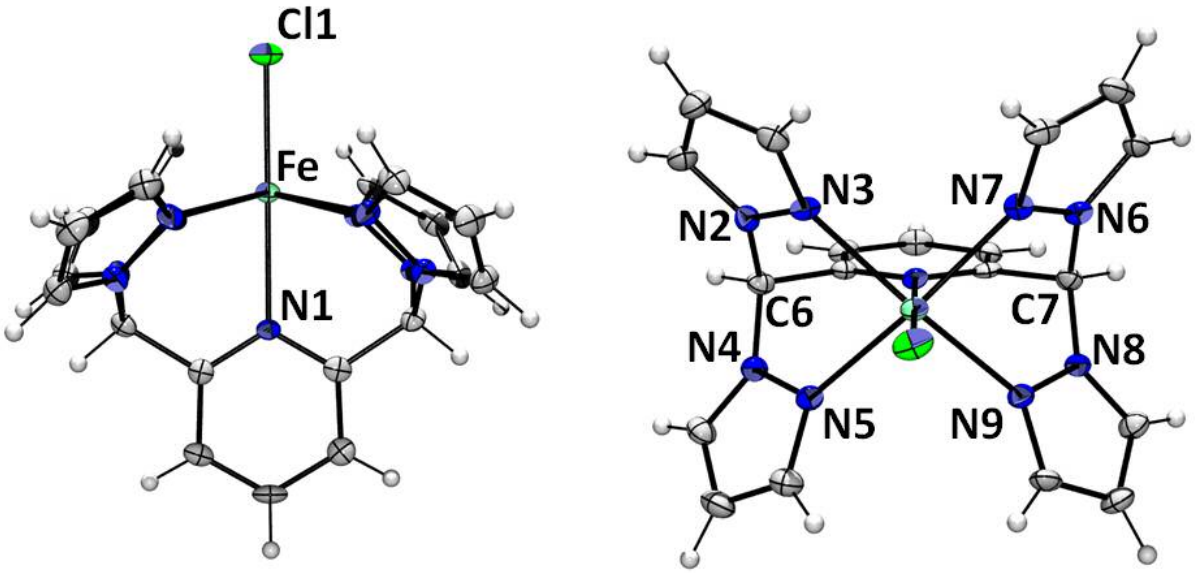

Views of Cation with Select Atom Labels

Figure S5. ORTEP diagrams (50% probability ellipsoids) of [CoCl(**pz$_4$lut**)](Cl)•CH_2Cl_2.

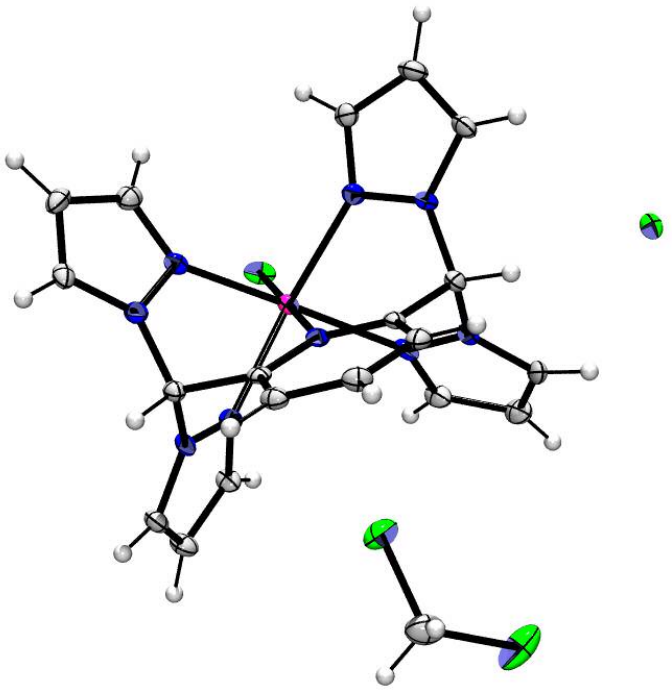

Asymmetric Unit

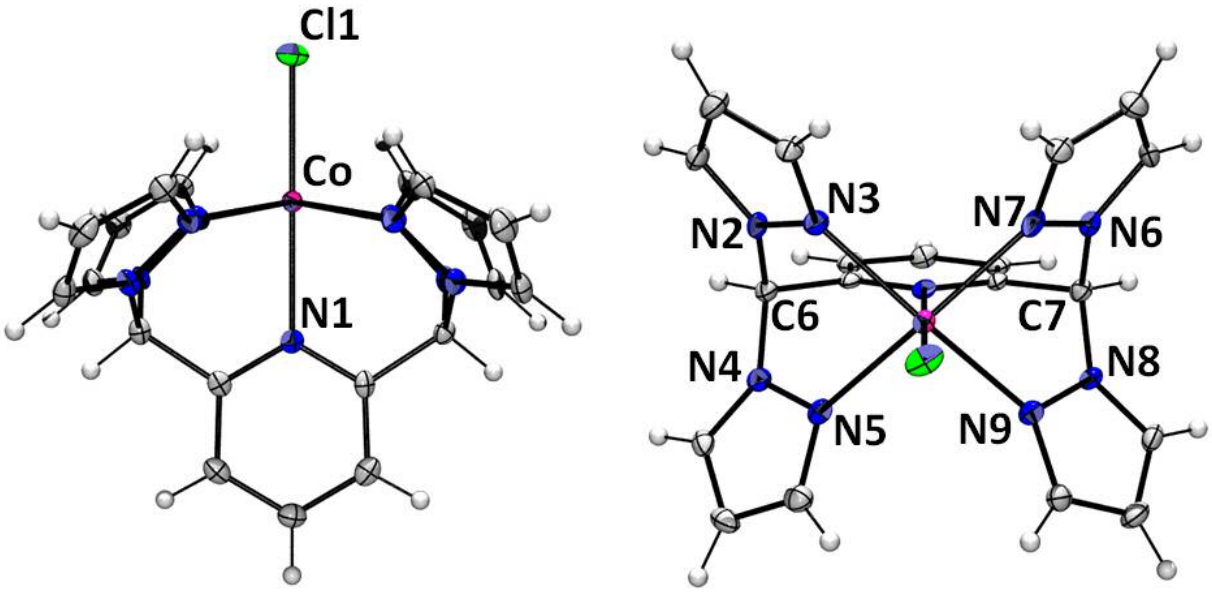

Views of Cation with Select Atom Labels

Figure S6. ORTEP diagrams (50% probability ellipsoids) of [NiCl(**pz$_4$lut**)](Cl)•EtOH.

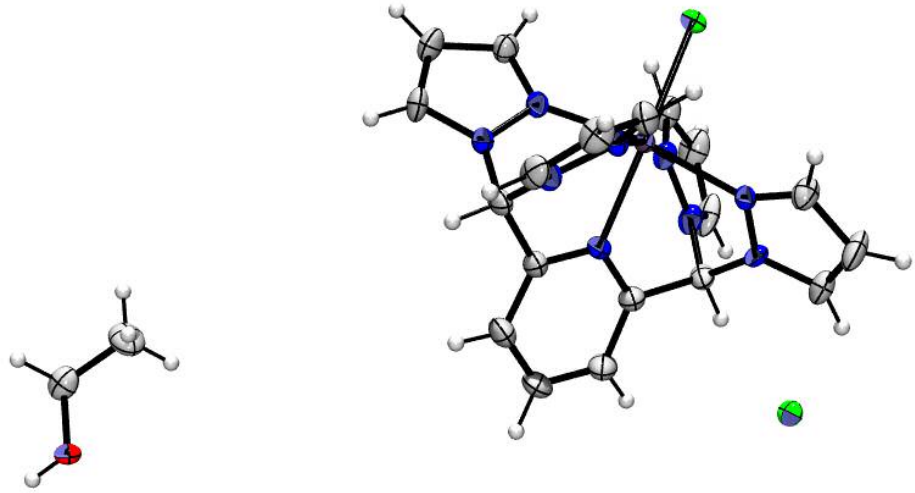

Asymmetric Unit (with anion and solvent disorder components removed)

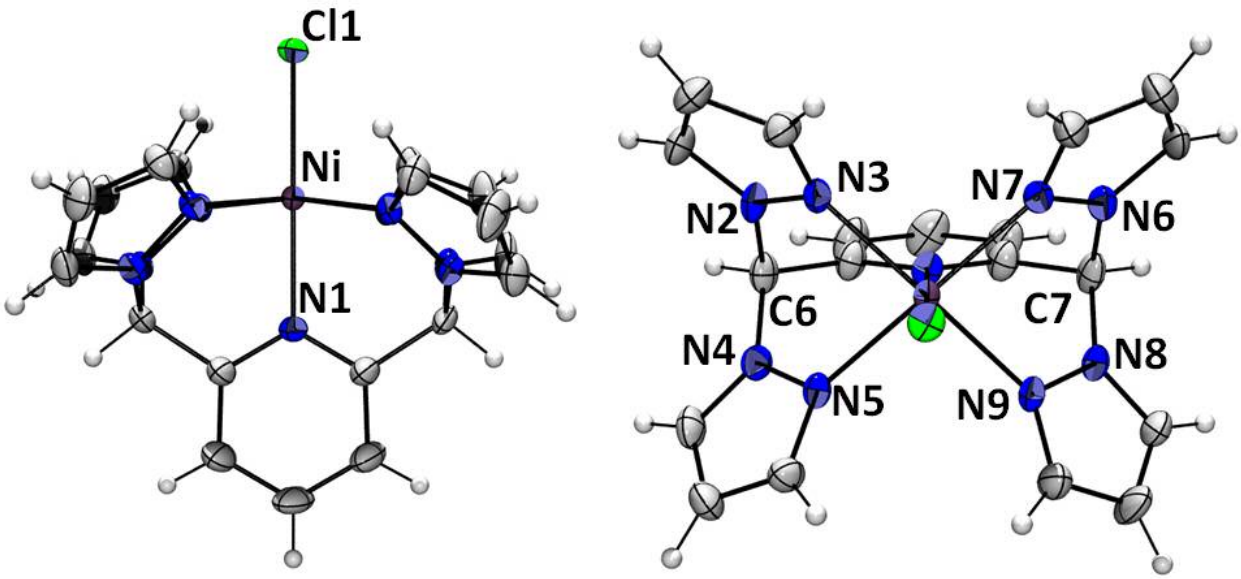

Views of Cation with Select Atom Labels

Figure S7. ORTEP diagrams (50% probability ellipsoids) of [CuCl(**pz$_4$lut**)](Cl)•0.82CH_2Cl_2.

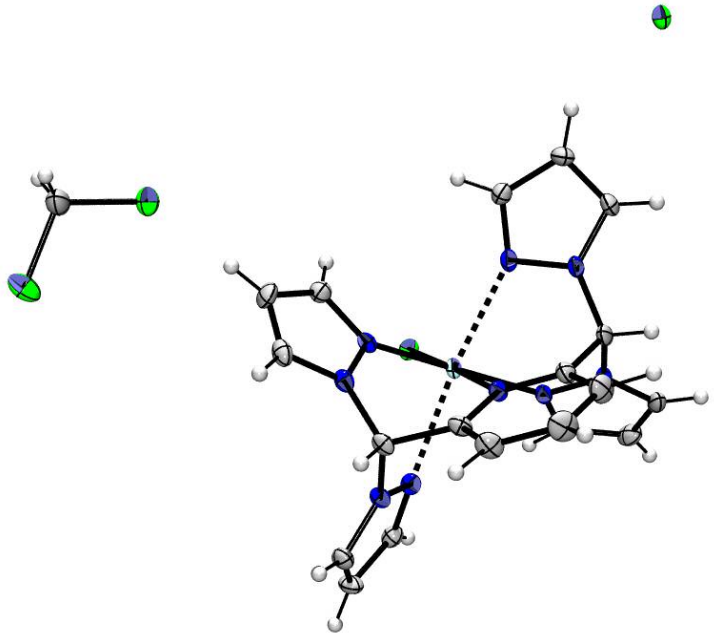

Asymmetric Unit

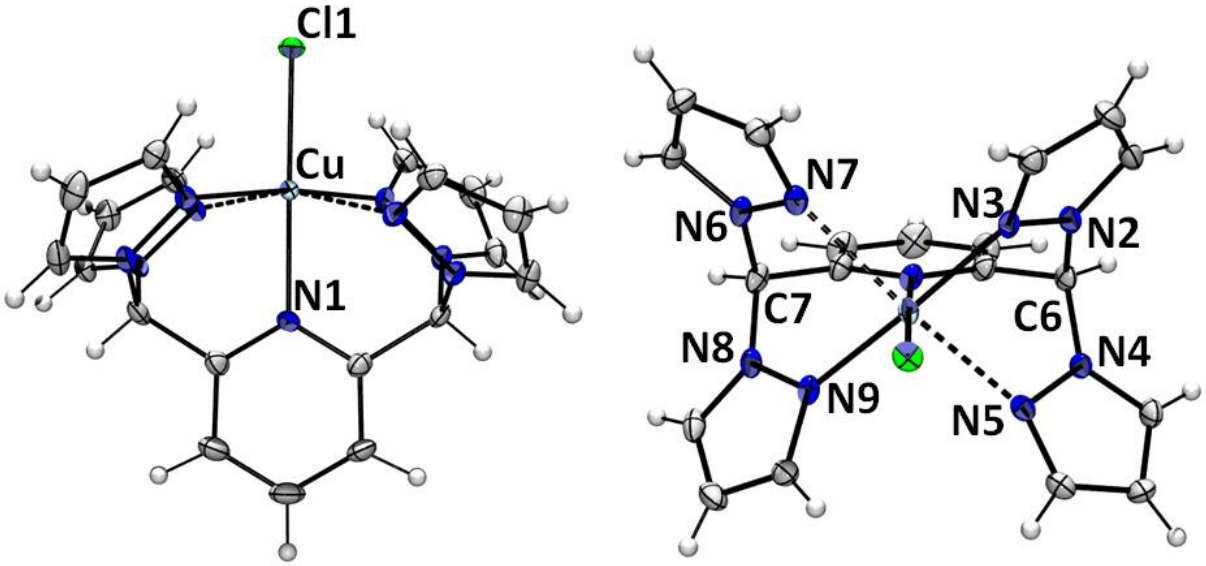

Views of Cation with Select Atom Labels

Figure S8. ORTEP diagrams (50% probability ellipsoids) of [ZnCl(**pz$_4$lut**)][ZnCl$_3$(MeOH)]•0.63 CH_2Cl_2•0.34 MeOH.

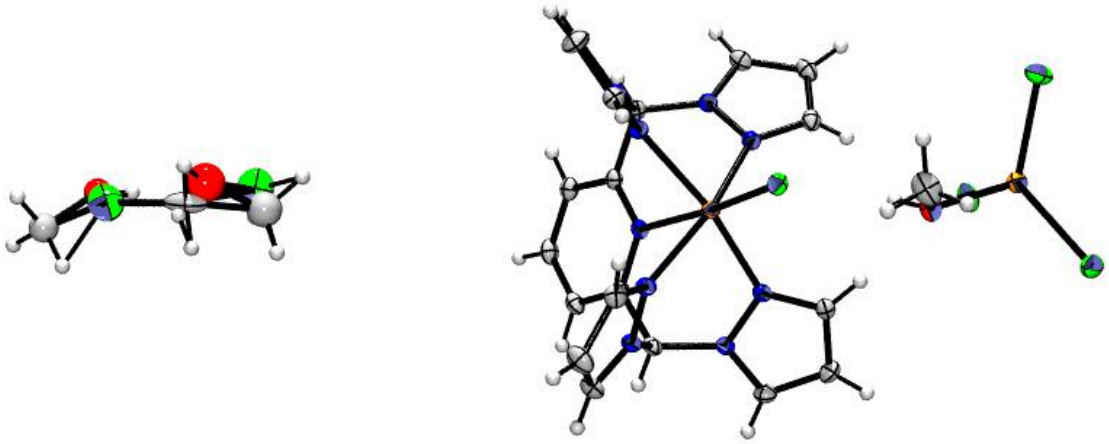

Asymmetric Unit

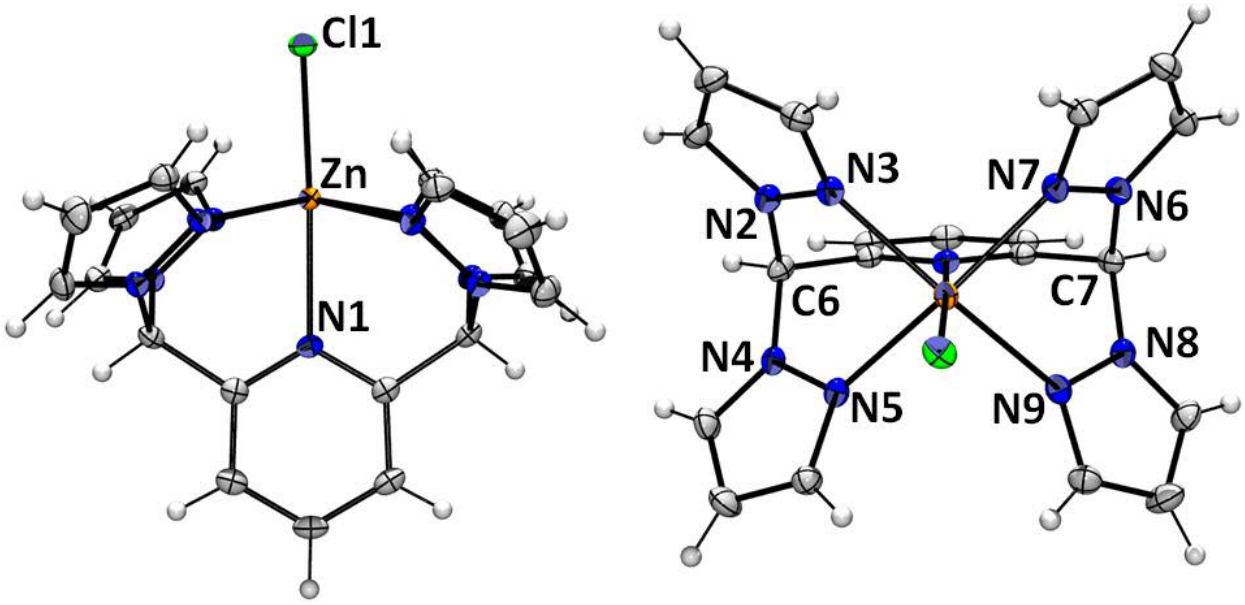

Views of Cation with Select Atom Labels

Figure S9. UV-Vis spectrum of **pz$_4$lut** in MeOH.

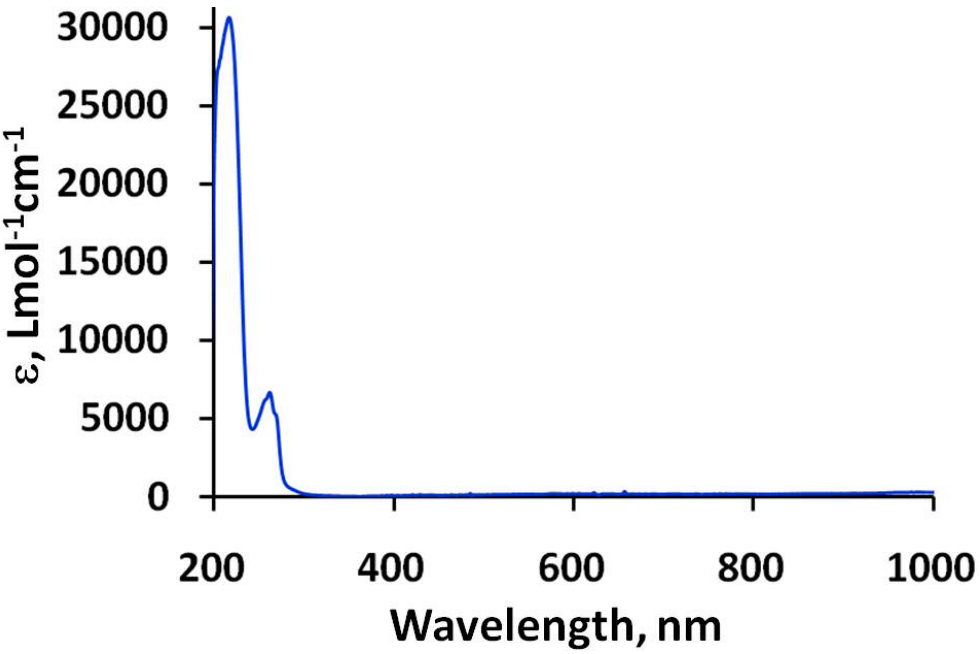

Figure S10. UV-Vis/NIR spectrum of [MnCl(**pz$_4$lut**)](Cl)•CH_2Cl_2 in MeOH.

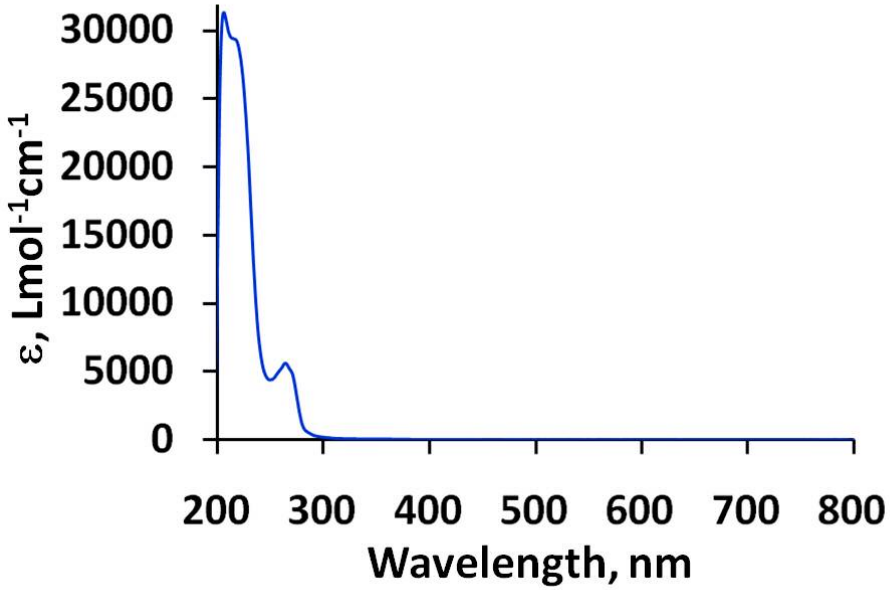

Figure S11. UV-Vis/NIR spectrum of [FeCl(**pz$_4$lut**)](Cl)•CH_2Cl_2 in MeOH.

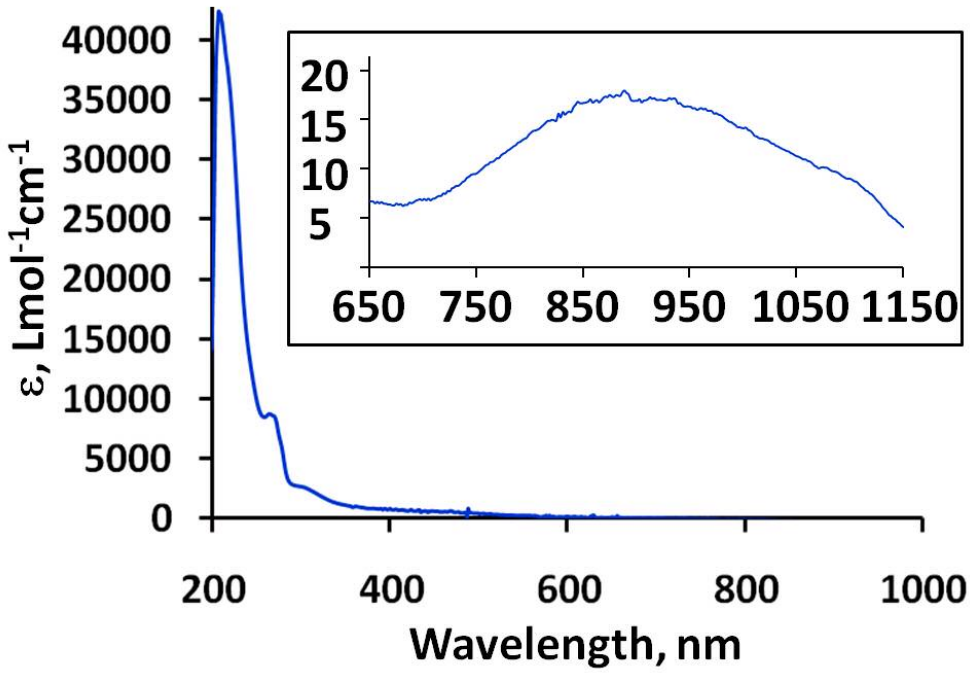

Figure S12. UV-Vis/NIR spectrum of [CoCl(**pz$_4$lut**)](Cl)•CH_2Cl_2 in MeOH.

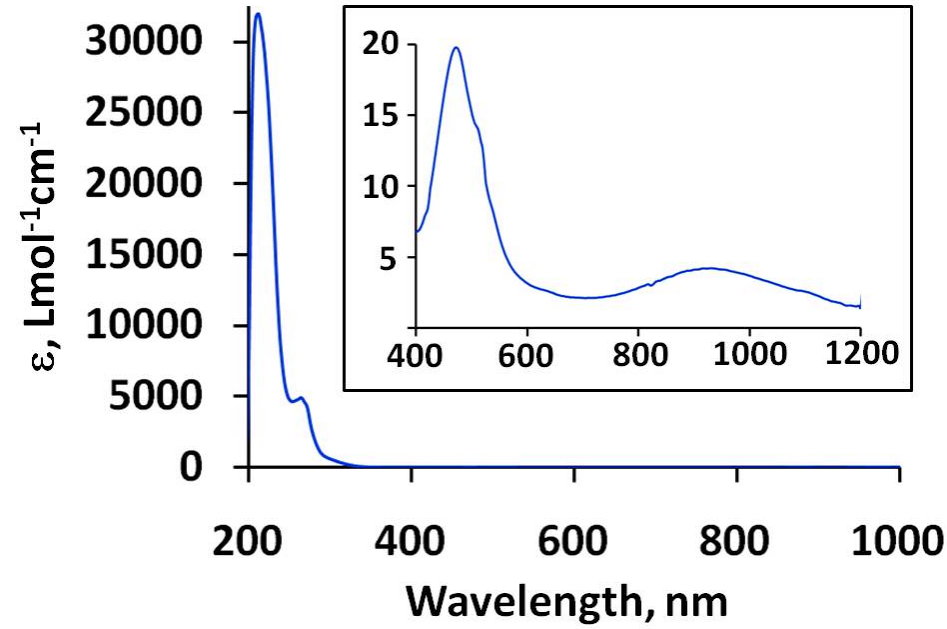

Figure S13. UV-Vis/NIR spectrum of [NiCl(**pz$_4$lut**)](Cl)•EtOH in MeOH.

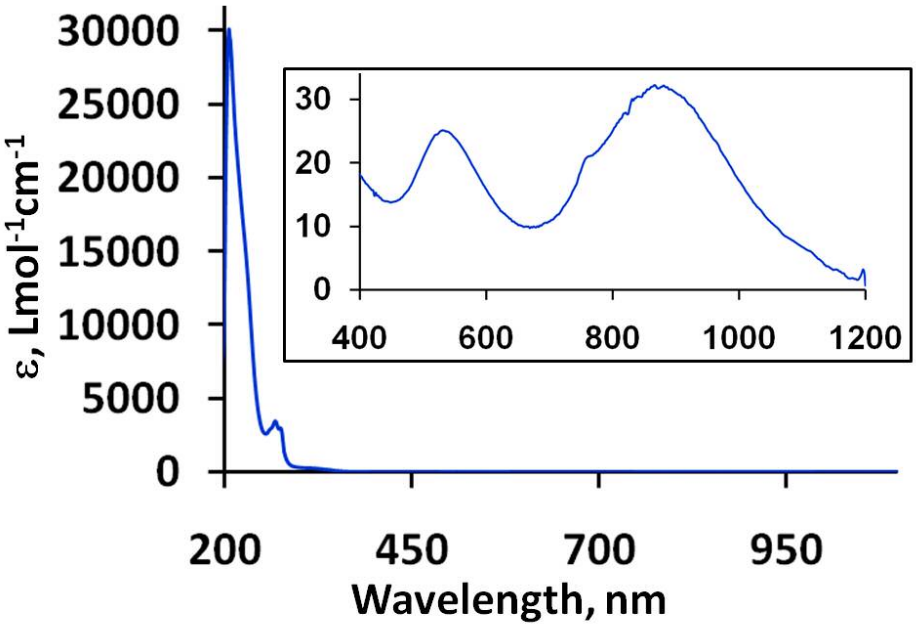

Figure S14. UV-Vis/NIR spectrum of [CuCl(**pz$_4$lut**)](Cl) in MeOH.

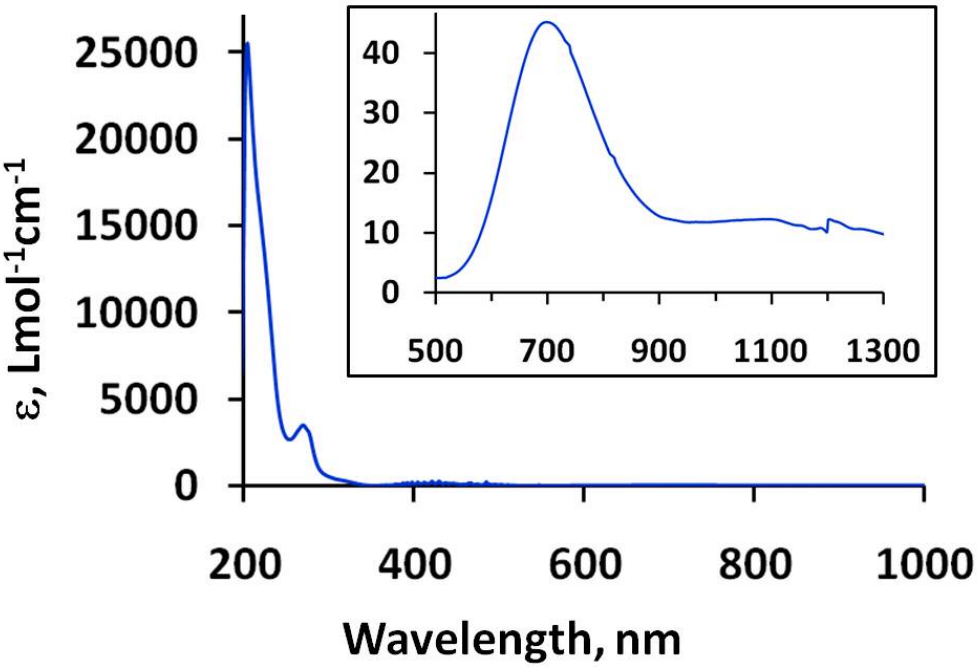

Figure S15. UV-Vis/NIR spectrum of [ZnCl(**pz$_4$lut**)][ZnCl$_3$(MeOH)] in MeOH.

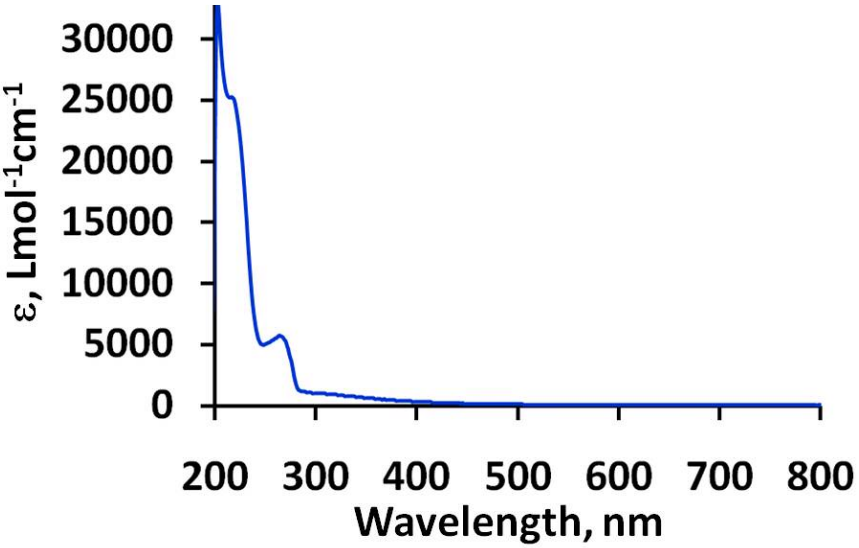

Figure S16. EPR spectra of [MnCl(**pz$_4$lut**)](Cl)•CH_2Cl_2 as a frozen dispersion in silicone oil. Transitions at g_{eff} ~ 10, 6 and 2 would be expected for a perfectly axial (*E/D* = 0) system with 7 cm^{-1} (10 K) > Δ >> 0.3 cm^{-1}. The complexity of the spectrum suggests that either the zero-field splitting is not sufficiently large that the Zeeman interaction can be treated as a perturbation (*i.e.* $\Delta \approx 0.3$ cm^{-1}), and/or that there is a significant rhombic zero field splitting term (*E/D* > 0).

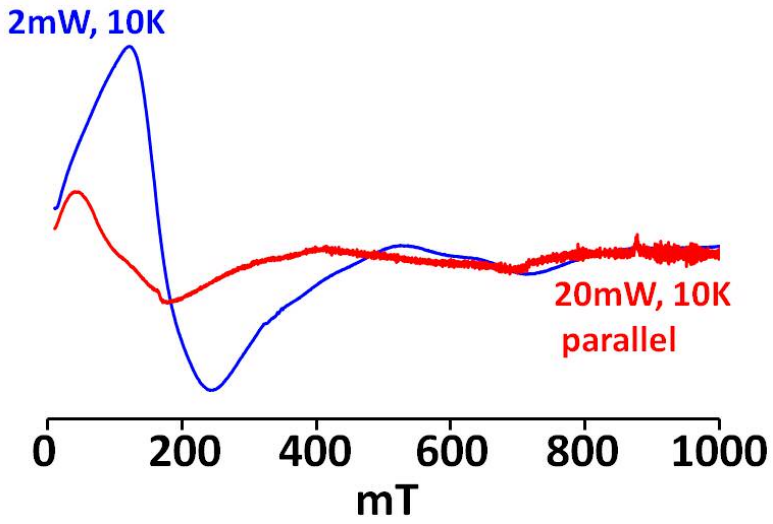

Figure S17. EPR spectra of [FeCl(**pz$_4$lut**)](Cl)•CH_2Cl_2 as a frozen dispersion in silicone oil. The parallel mode signal at g_{eff} ~ 9 is due to Fe(II), the dominant species. The perpendicular mode signal reveals traces of Fe(III)

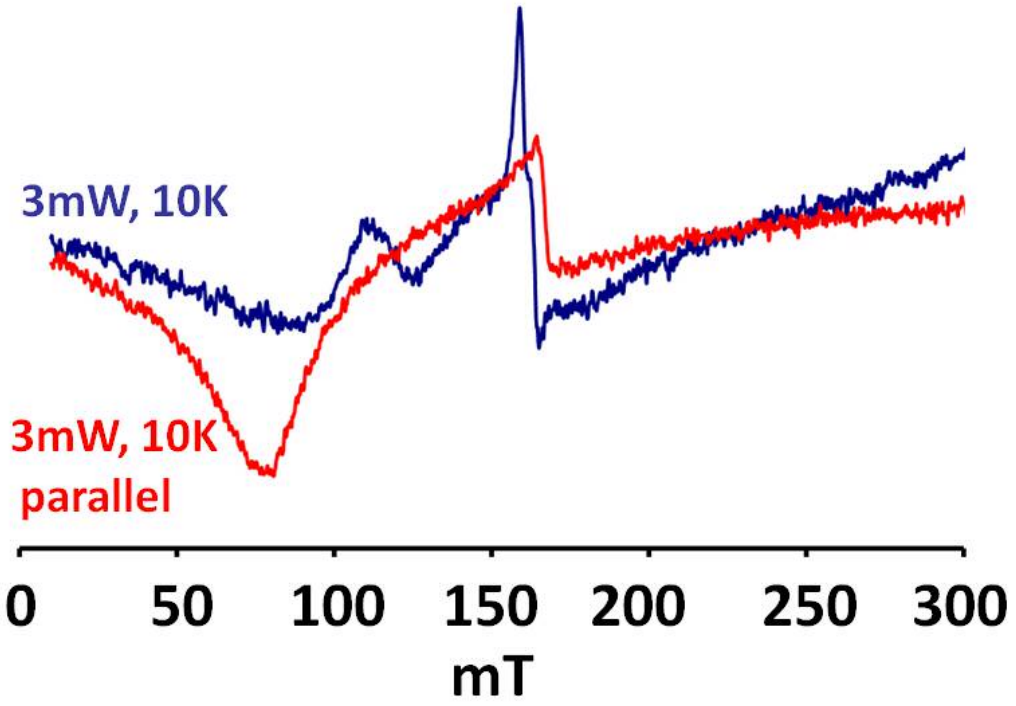

Figure S18. EPR spectra of [CoCl(**pz$_4$lut**)](Cl)•CH_2Cl_2 as a frozen dispersion in silicone oil. The major resonances at g_{eff} = 4.3 and 2.3 indicate $S = {}^3/_2$ with $\Delta >> g\beta BS$ and $M_S = |\pm{}^1/_2\rangle$. The small feature at g_{eff} = 11.5 is likely due to spin-spin interaction between Co(II) ions (S = 0, 1, 2, 3).

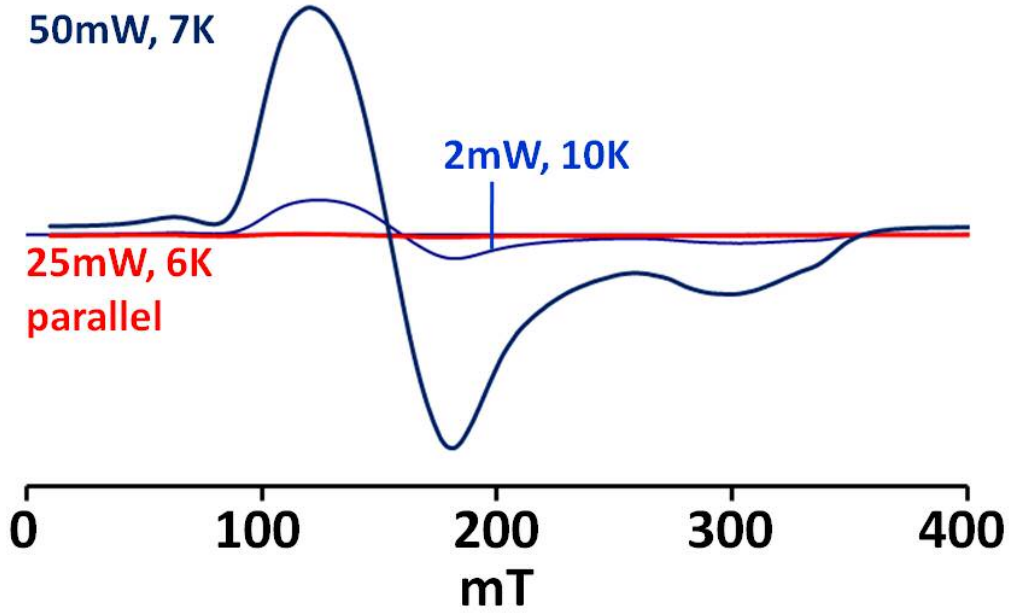

Figure S19. EPR spectra of [CuCl(**pz$_4$lut**)](Cl) as a frozen dispersion in silicone oil. $g_{||}$ and $A_{||}$ are indicative of nitrogen ligation of Cu(II). The shoulder to the high field side of the main $g_{\perp}$ peak, and it's partner to the low field side, are due to dipolar interaction between adjacent Cu(II) ions.